

Optimizing the lateral beamforming step for filtered-delay multiply and sum beamforming to improve active contour segmentation using ultrafast ultrasound imaging

Asraf Mohamed Moubark^{a,*}, Zainab Alomari^b, Mohd Hairi Mohd Zaman^a,
Mohd Asyraf Zulkifley^a, Sawal Hamid Md Ali^a, Luzhen Nie^c, Steven Freear^c

^a Department of Electrical, Electronic and Systems Engineering, Faculty of Engineering and Built Environment, Bangi Selangor 43600, Malaysia

^b Department of Communications Engineering, Electronics Engineering College, Ninevah University, Mosul 41002, Iraq

^c Ultrasonics and Instrumentation Group, School of Electronic and Electrical Engineering, University of Leeds, Leeds LS2 9JT, United Kingdom

ARTICLE INFO

Keywords:

Active contours
Autocorrelation beamforming
Compounding
Delay and sum
Filtered-delay multiply and sum
Ultrafast imaging
Segmentation

ABSTRACT

As an alternative to delay-and-sum beamforming, a novel beamforming technique called filtered-delay multiply and sum (FDMAS) was introduced recently to improve ultrasound B-mode image quality. Although a considerable amount of work has been performed to evaluate FDMAS performance, no study has yet focused on the beamforming step size, Δx , in the lateral direction. Accordingly, the performance of FDMAS was evaluated in this study by fine-tuning Δx to find its optimal value and improve boundary definition when balloon snake active contour (BSAC) segmentation was applied to a B-mode image in ultrafast imaging. To demonstrate the effect of altering Δx in the lateral direction on FDMAS, measurements were performed on point targets, a tissue-mimicking phantom and *in vivo* carotid artery, by using the ultrasound array research platform II equipped with one 128-element linear array transducer, which was excited by 2-cycle sinusoidal signals. With 9-angle compounding, results showed that the lateral resolution (LR) of the point target was improved by 67.9% and 81.2%, when measured at -6 dB and -20 dB respectively, when Δx was reduced from λ to $\lambda/5$. Meanwhile the image contrast ratio (CR) measured on the CIRS phantom was improved by 10.38 dB at the same Δx reduction and the same number of compounding angles. The enhanced FDMAS results with lower side lobes and less clutter noise in the anechoic regions provides a means to improve boundary definition on a B-mode image when BSAC segmentation is applied.

1. Introduction

The computation effective nature of delay-and-sum (DAS) beamforming makes it a popular option for medical ultrasound imaging. However, DAS fails to eliminate clutter noise [1–3]. This condition leads to a low contrast ratio (CR) and poor spatial resolution. Considerable work has been conducted to combat poor image quality encountered by DAS, such as improving the beamforming algorithm with pre/post-signal processing techniques or replacing it with new algorithms [4,12,1,5].

Lim et al. introduced a novel beamforming technique called delay multiply and sum (DMAS) [6]. This technique has been applied to radar microwave imaging for detecting breast cancer where the main

objective is to find the tumour with a CR between 2:1 and 10:1 relative to normal breast tissue [7–10]. Thus, this method is unsuitable for ultrasound imaging which comprises several signal levels: hyperechoic, isoechoic, hypoechoic and anechoic. Matrone et al. [11] modified and improved the algorithm by introducing new mathematical blocks and named it the filtered DMAS (FDMAS) algorithm. This new beamforming technique achieves higher image CR and better lateral resolution (LR) with less computation compared with adaptive beamforming techniques [12].

Matrone et al. applied FDMAS to linear array imaging (LAI), synthetic aperture focusing (SAF), multi-line transmission (MLT) and plane wave imaging (PWI) [13–15]. The application of FDMAS to LAI improves image LR and CR. The axial resolution is retained but the

* Corresponding author.

E-mail addresses: asrafmohamed@ukm.edu.my (A.M. Moubark), zainab.saleh@uoninevah.edu.iq (Z. Alomari), hairizaman@ukm.edu.my (M.H. Mohd Zaman), asyraf.zulkifley@ukm.edu.my (M.A. Zulkifley), sawal@ukm.edu.my (S.H. Md Ali), l.nie@leeds.ac.uk (L. Nie), s.freear@leeds.ac.uk (S. Freear).

<https://doi.org/10.1016/j.bspc.2021.103267>

Received 24 November 2020; Received in revised form 5 October 2021; Accepted 15 October 2021

Available online 29 October 2021

1746-8094/© 2021 The Author(s).

Published by Elsevier Ltd.

This is an open access article under the CC BY-NC-ND license

(<http://creativecommons.org/licenses/by-nc-nd/4.0/>).

contrast-to-noise (CNR) ratio is degraded compared with DAS. The spatial lateral resolution and CR can be improved when FDMAS is applied to SAF and MLT. Reduction of crosstalk noise is also demonstrated in latter applications.

Despite the significant amount of research reported on FDMAS, no in-depth investigation has been conducted on the effect of varying the beamforming step size, Δx , in the lateral direction, which is one of the important criteria for determining B-mode image quality. In a previous study [16] on compound PWI (CPWI) with DAS beamforming, the evaluation of the final B-mode image quality did not exhibit any significant variations, except reduction on the grating lobes when different inter-element spacings or pitch sizes, p (λ or $\lambda/2$), were used whilst maintaining other experimental parameters. The LR measured on the point targets at full width at half maximum (-6 dB) from a depth of 10 mm to 60 mm obtained using imaging probes with pitch sizes of λ and $\lambda/2$ are nearly the same. Moreover, the CR values measured using probes with pitch sizes of λ and $\lambda/2$ on a cyst with a depth ranging from 20 mm to 60 mm do not exhibit any significant difference. This previous study also showed that grating lobes when using a probe with a pitch size of λ , can be effectively reduced through compounding. Furthermore, grating lobes mainly appear in the near-field regions (≤ 10 mm). The final outcome of [16] provides a strong hypothesis that the Δx plays an important role in determining the final quality of the B-mode image. This finding has motivated us to further explore the effect of varying Δx with the recently proposed FDMAS beamforming techniques primarily because the FDMAS algorithm is similar to the autocorrelation process that depends on the lag among radio-frequency (RF) signals in each channel in the lateral direction. Thus, the proper selection of Δx for FDMAS is a subject for discussion.

The enhanced FDMAS with lower side lobes and less clutter noise is expected to improve the balloon snake active contour (BSAC) segmentation process. Segmentation is a process of partitioning an image in which the intended region of interest (ROI) can be distinguished from the background [17], BSAC is a popular segmentation method that has been used in medical ultrasound imaging [18,19]. Segmenting complex topology such as a blood vessel in retinal angiography and cerebral cortex structures manually are not feasible and time consuming [20]. Segmenting the carotid artery wall is also one of the first procedures before any measurements can be performed. This process can either involve measuring the diameter of the common carotid artery (CCA) or the intima media thickness. Moreover, clutter noise and side lobes in anechoic regions are known obstacles to exact boundary definition during BSAC segmentation [21]. Attenuating noise and side lobes by enhancing FDMAS could promise improved boundary delineation.

In this study, we investigated the effect of varying the Δx , on CPWI for point targets, a tissue-mimicking phantom and an *in vivo* carotid artery. This study is expected to propose the optimized Δx for FDMAS to improve B-mode image quality for better boundary definition using BSAC segmentation.

2. Materials and methods

2.1. Coherent PWI

To achieve the same quality as a focused image at point located at z mm depth, N steered plane waves (n) are required [22,23]:

$$N = \frac{L_a}{\lambda F} = \frac{L_a^2}{\lambda z}, \quad (1)$$

where L_a is the length of the aperture, λ is the signal wavelength and F is the F-number defined as $F = z/L_a$. Each steering angle, θ_n , is given by

$$\theta_n = \arcsin\left(\frac{n\lambda}{L_a}\right) \approx \left(\frac{n\lambda}{L_a}\right), \quad (2)$$

where n is defined as

$$n = \left[-\frac{N-1}{2}, \dots, \frac{N-1}{2} \right]. \quad (3)$$

The main objective of this work is to evaluate the effect of varying Δx on imaging results when using any number of compounding angles with the DAS and FDMAS beamforming techniques, and not to find the optimum number of compounding angles in CPWI. Many studies, including [24,25,23,16], have proposed a unique number of compounding angles that provide the best image quality according to their experimental setup. Thus, a particular compounding angle that will provide the best end results for all image quality indices is impossible to propose. The general rule of thumb in selecting the number of compounding angles is to minimize it, such that the end results are balanced among the optimum temporal, spatial and contrast resolutions. Several studies, such as [24,25], have mentioned that beyond a certain number of compounding angles, image resolution will no longer improve but will deteriorate instead due to reduced noise cancellation near the main lobe. In consideration of these constraints, the selected number of compounding angles, N , and the steering angle increment, $\Delta\theta_n$, are shown in Table 1. The sector angles, $[\theta_{max}^o, \theta_{min}^o]$, for all compounding conditions are set to $\pm 12^\circ$.

2.2. FDMAS beamforming

The initial process in FDMAS is the same as that in DAS. Here, the signal $s_i(t)$ is the RF signal received by each element, i . To temporarily align the signals received by each element, the following equation is used to calculate the required focusing delay, τ_i [45,44]:

$$\tau_i(x_g, \mathbf{Z}) = \frac{Z \cos\theta_n + x_g \sin\theta_n + \frac{L_a}{2} \sin\theta_n}{c} + \frac{\sqrt{Z^2 + (x_i - x_g)^2}}{c}, \quad (4)$$

where x_g is the imaging point in the lateral direction for a lateral beamforming step of λ/g , where $g = 1, 2, 3, 4$ and 5. This can be further elaborated as $x_1 = \lambda, 2\lambda \dots L_a$; $x_2 = \lambda/2, \lambda \dots L_a$ and so on and so forth. While \mathbf{Z} is the vector of imaging points in the axial direction given by

$$\mathbf{Z} = \begin{bmatrix} z_1 \\ z_2 \\ \vdots \\ z_{depth} \end{bmatrix} \quad (5)$$

where z_{depth} is the maximum imaging depth, c is the speed of sound of the medium, and x_i is the distance between the i_{th} element and the center of the transducer. The RF signal with the focusing delay compensated, $s_i(x_g, \mathbf{Z})$, is known as the aligned RF signal, $v_i(x_g, \mathbf{Z})$, and can be represented by the following equation:

$$v_i(x_g, \mathbf{Z}) = s_i(t - \tau_i(x_g, \mathbf{Z})). \quad (6)$$

Differs from DAS, the aligned signals in DMAS will undergo a process similar to autocorrelation, which can be represented by the following equation [11]:

$$r_{DMAS}(x_g, \mathbf{Z}) = \sum_{i=1}^{E-1} \sum_{m=i+1}^E \text{sgn}\{v_i(x_g, \mathbf{Z})v_m(x_g, \mathbf{Z})\} \times \sqrt{|v_i(x_g, \mathbf{Z})v_m(x_g, \mathbf{Z})|}, \quad (7)$$

where E is the total number of elements on the imaging probe, and $m = i+1$ is the aligned RF signal at the m -th element. The multiplication

Table 1
Compounding parameters.

Properties	Value						
Number of Compounding Angles, N	1	3	5	7	9	13	25
Angle Increment, $\Delta\theta_n$	0	12	6	4	3	2	1

of two RF signals with the same frequency content will eventually produce the second harmonic and direct current components. Thus, a band-pass filter is applied to $r_{\text{DMAS}}(x_g, Z)$ to extract its second harmonic, and finally, $r_{\text{FDMAS}}(x_g, Z)$ is obtained. For a fixed lateral location x_g , a set of time delays are calculated for each depth Z , to form a vertical imaging line, l .

2.3. Beamforming step size, Δx

The effect of varying Δx during beamforming on B-mode image quality was studied by first calculating the difference in the imaging line angle, $\Delta\beta_g$ between the first and second imaging line angles and then calculating the correlation coefficient, ρ_g between two adjacent aligned RF signals from the first ($i = 1$) and second ($i = 2$) elements for the first imaging line. Fig. 1 illustrates the concept of imaging line angle and imaging line produced with different Δx . Δx is also referred to as the lateral beamforming step which is given by

$$\Delta x = x_g(k+1) - x_g(k) = \lambda/g \quad (8)$$

where $x_g(k)$ and $x_g(k+1)$ are the k th and $k+1$ th imaging points in the lateral direction. $\Delta\beta_g$ is given by

$$\Delta\beta_g = \beta_{(l+1)_g}^o - \beta_l^o; \quad (9)$$

where $\beta_{(l+1)_g}^o$ and β_l^o are the l th and $l+1$ th imaging line angles formed between a set of aligned RF signals and the surface of the transducer. $\Delta\beta_g$ for the Δx , λ and $\lambda/4$, are given by

$$\begin{aligned} \Delta\beta_1 &= \beta_{2_1}^o - \beta_{1_1}^o, \quad \text{for } \lambda; \\ \Delta\beta_4 &= \beta_{2_4}^o - \beta_{1_4}^o, \quad \text{for } \lambda/4; \\ \Delta\beta_1 &> \Delta\beta_4; \end{aligned} \quad (10)$$

where $\beta_{1_1}^o$ and $\beta_{2_1}^o$ are the imaging line angles for the aligned RF signals for the first imaging line and the second imaging line for the Δx of λ . $\beta_{1_4}^o$

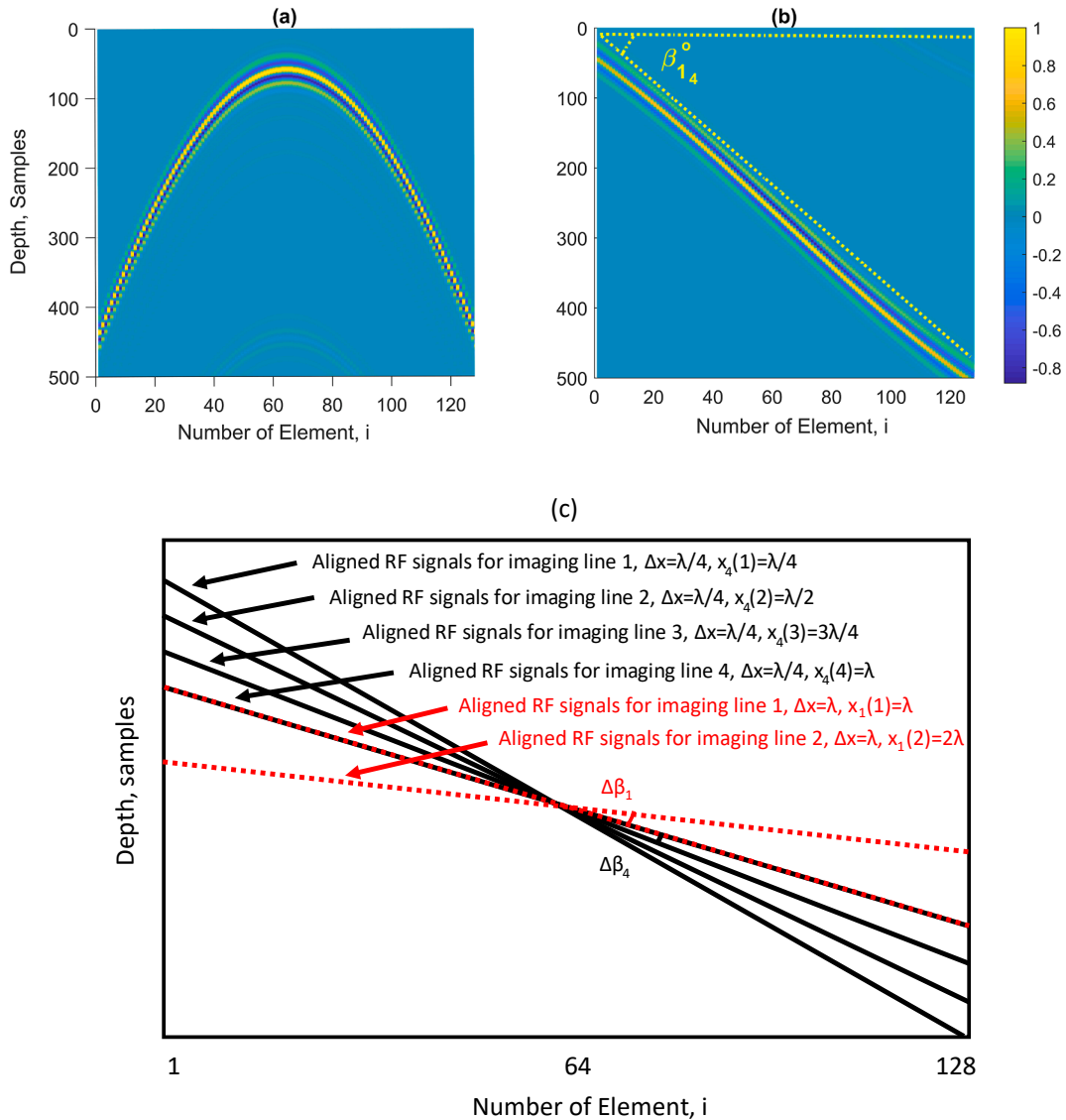


Fig. 1. a) The RF echo originated from a scattering point located at center of the imaging medium at 40 mm depth. b) RF signals for $E = 128$ elements aligned according to Eq. (6) for imaging line 1 with the Δx of $\lambda/4$. $\beta_{1_4}^o$ formed between the face of the imaging probe and the aligned RF signals is highlighted. c) Aligned RF signals for imaging lines 1 and 2 for the Δx of λ and aligned RF signals for imaging lines 1, 2, 3 and 4 with the Δx of $\lambda/4$ are shown together with differences between the imaging line angles, $\Delta\beta_1$ and $\Delta\beta_4$ respectively.

and $\beta_{2_4}^0$ are the imaging line angles for the aligned RF signals for the first imaging line and the second imaging line for the Δx of $\lambda/4$. To illustrate the new concept of Δx and $\Delta\beta_g$ in this work, a Field II simulation with the parameters listed in Table 3 was performed. Echoes from a scattering point located at 40 mm depth were obtained by transmitting an unsteered plane wave. Both $\Delta\beta_g$ and $\beta_{1_4}^0$ formation are shown in Fig. 1(b) and (c). $\beta_{1_4}^0$ measured after the received RF echo aligned according to Eq. (6). In Fig. 1(b) the RF echo aligned for the first imaging line with the Δx of $\lambda/4$ is shown. Accordingly, $\beta_{1_4}^0$ formed between the face of the imaging probe and the aligned RF signals is highlighted as $\beta_{1_4}^0$.

The correlation coefficient, ρ_g , between two aligned RF signals from the first and second elements is computed on the first imaging line for every Δx according to the following equation [26]

$$\rho_g = \frac{v_1(x_g, \mathbf{Z})v_2(x_g, \mathbf{Z})}{\sqrt{v_1(x_g, \mathbf{Z})^2 v_2(x_g, \mathbf{Z})^2}} \quad (11)$$

where $v_1(x_g, \mathbf{Z})$ and $v_2(x_g, \mathbf{Z})$ are the aligned RF signals from the first ($i=1$) and second ($i=2$) elements as given by Eq. (6). In digital signal processing, the autocorrelation between two signals is calculated at a lag that is relative to the starting point of one of the signals. The lag refers to as the distance or location shift between two points. The multiplication of two RF signals and then summing them at a specific lag is known as short-time autocorrelation [27]. The lag is commonly represented in the form of the samples. However, in this work the lag is assigned to be the angle difference, $\Delta\beta_g$, between two imaging line angles. The lag between adjacent RF signals along the lateral direction depends on Δx . The number of times the RF signals of all the elements should be aligned to form imaging lines for the same lateral distance increases as Δx is reduced. Instead of aligning all the RF signals of all the elements at one time with the Δx of λ , all the RF signals will now be aligned twice with the Δx of $\lambda/2$. Simultaneously, instead of assigning a single grey colour intensity on a particular imaging point, two different grey colour intensities will be assigned with the Δx of $\lambda/2$ on two different imaging points. The length of an imaging point with the Δx of λ is equal to two imaging points with the Δx of $\lambda/2$.

Some linear array transducers available in the market are provided in Table 2. They are used for research purposes and have a pitch size of p , that is equal to or higher than the wavelength λ . The optimization of Δx for such probes is expected to improve B-mode image quality.

2.4. Snake active contour segmentation

Snake active contour-based segmentation techniques begin with the user-defined approximate boundary, known as a contour, around an object. Thereafter the initial contour will evolve and determine the actual boundary of the object. The objective of snake active contour formation is to minimise the combined internal energy (contour shape) and external energy (image gradient) by continuously evolving within a certain number of iterations. At each iteration, the total snake energy is computed such that it will always be the minimum. The total snake energy can be minimised through the calculus of the variation by solving the following Euler–Lagrangian equation [17]:

Table 2
Specification of transducers.

Properties	Prosonics	Verasonics	Verasonics
Model	L3-8/40EP	L3-12-D	L11-4v
Centre Frequency, MHz	4.79	6.5	7.55
Bandwidth (–6 dB), %	57	85	90.8
Element Pitch, mm	0.3048	0.2	0.298–0.302
Element Pitch, λ	1.01	1.18	0.66–0.65

$$\frac{\delta}{\delta s}(\alpha(s)V_s(s)) + \frac{\delta^2}{\delta s^2}(\beta(s)V_{ss}(s)) - \nabla E_{\text{ext}}(V(s)) = 0, \quad (12)$$

where $s \in [0, 1]$ represents points on the contour, $V(s)$. The first derivative, $V_s(s)$ provides a measure of the elasticity (stretching) strength of the contour control via $\alpha(s)$, whereas the second derivative, $V_{ss}(s)$ provides a measure of the rigidity (bending) strength of the contour control via $\beta(s)$. $E_{\text{ext}}(V(s))$ is the external energy of an image.

2.5. Experimental setup

To validate the effect of varying Δx on the FDMAS beamforming technique, several measurements were performed on point targets with a diameter of 120 μm , a tissue-mimicking phantom (040GSE, CIRS, Virginia, USA) and *in vivo*. The anechoic sections of the tissue-mimicking phantom (depth: 10 mm to 50 mm) and the point targets (depth: 10 mm to 70 mm) were imaged. *In vivo* data were collected from the cross section of the right common carotid artery of a healthy volunteer. A 128-element linear array transducer (L3-8/40EP, Prosonics Co. Ltd., South Korea) with a center frequency of 4.79 MHz and a 57% bandwidth at –6 dB was used to collect all the data. A two-cycle sinusoidal excitation signal at a center frequency of 5 MHz was used with the ultrasound array research platform II (University of Leeds, UK) [28–30]. The received signals were sampled at 80 MHz. The complete experimental parameters are provided in Table 3.

3. Performance evaluation

The performance of the final B-mode images produced using the DAS and FDMAS beamforming techniques can be described by two main matrices: spatial resolution and CR. To determine image LR, the main lobes of the point target represented by the nylon wire with a diameter of 120 μm at a depth of 40 mm in degassed and deionised water were measured at –6 dB and –20 dB using the function developed in [31]. The CR was used to express the detectability of a cyst with values between the ROI inside the cyst and its background. While CNR is used to measure the cyst contrast with speckle or noise variation inside and outside of the cyst. The image CR and CNR of the anechoic cyst of 3.0 mm diameter located at a depth of 15 mm were computed by creating two regions with the same dimensions. The first region is located inside the cyst, whereas the second region is located outside the cyst at the same depth. This condition ensures that attenuation with depth does not affect the measurements. The CR and CNR equations are given as follows [11,1]

$$\text{CR(dB)} = 20\log_{10}\left(\frac{\mu_{\text{cyst}}}{\mu_{\text{back}}}\right), \quad (13)$$

$$\text{CNR(dB)} = 20\log_{10}\left(\frac{|\mu_{\text{cyst}} - \mu_{\text{Back}}|}{\sqrt{(\sigma_{\text{cyst}}^2 + \sigma_{\text{Back}}^2)}}\right) \quad (14)$$

where μ_{cyst} and μ_{Back} are the means of image intensities inside and

Table 3
Simulation and experimental parameters.

Properties	Values
Speed of Sound, Water/CISR	1482/1540 m/s
Medium Attenuation, Water/CISR	0.002/0.5 dBcm ⁻¹ MHz ⁻¹
Number of Elements	128
Transducer Center Frequency	4.79 MHz
Transducer Bandwidth (–6 dB)	57 %
Transducer Element Pitch, p	0.3048 mm
Sampling Frequency, f_s for Tx/Rx	160/80 MHz
Excitation Signal	Two-cycle Sinusoid
Excitation Signal Center Frequency	5 MHz

outside of the cyst respectively, while σ_{cyst} and σ_{Back} are their variances. All results for simulations and experiments were presented in the form of mean value \pm one standard deviation, calculated based on 10 repeats of measurements. The transducer was not moved along the elevation direction during the repeated measurements.

4. Results and discussion

4.1. Simulation results

$\Delta\beta_g$ between the first and second imaging lines and ρ_g between RF signals on the first and second elements for the first imaging line calculated for the Δx , from λ to $\lambda/5$ for the pitch size, p , of λ and $\lambda/2$ are illustrated in Fig. 2. $\Delta\beta_g$, begins to decrease by reducing the Δx from λ to $\lambda/5$. For the pitch size of λ and the Δx of λ , $\Delta\beta_1$, between the first and second imaging lines is 0.8° . The Δx is reduced to $\lambda/5$, and thus $\Delta\beta_5$ becomes 0.21° . When $\Delta\beta_g$ starts to decrease, the correlation, ρ_g , between two adjacent RF signals will also decrease [27]. This situation shows that the two RF signals on adjacent elements are moving further apart. In accordance with Eq. (7), this condition will produce precise grey colour intensities at particular imaging points. FDMAS uses a nearly similar process to autocorrelation to compute the beamformed signals from the aligned RF signals. The reduction of Δx will enable FDMAS to beamform the received RF signals accurately. Thus, instead of assigning approximate grey colour intensity values on imaging points with fewer imaging lines, assigning more imaging lines with smaller imaging points will help define the exact or accurate intensity values at the smaller imaging points.

The results of the Field II simulation with the parameters listed in Table 3 are presented in Fig. 3 [32]. All the B-mode images are displayed within a 50 dB dynamic range. Fig. 3 shows the B-mode images of the point target located at 40 mm depth beamformed with a) DAS, $p = \lambda$, $E = 128$; b) FDMAS, $p = \lambda$, $E = 128$; c) DAS, $p = \lambda/2$, $E = 256$ and d) FDMAS, $p = \lambda/2$, $E = 256$. The beam profiles in Fig. 3 are shown in the lateral direction in Fig. 4. Regardless of the probe pitch size, p , the B-mode images exhibit the same outcomes when the Δx is set to $\lambda/2$. This important finding shows that the step size of imaging points plays an extremely important role in determining final image quality. Even with a larger pitch size, p , of λ , good-quality B-mode images can be produced with fewer number of elements, E , and shorter computational time compared with probes with the pitch size, p , of $\lambda/2$.

The number of pixels in the lateral direction produced with the Δx of $\lambda/2$ is twice that with the Δx of λ for a single B-mode image frame. As a drawback, however, reducing the Δx will increase the computational time of the beamforming process to form a B-mode image.

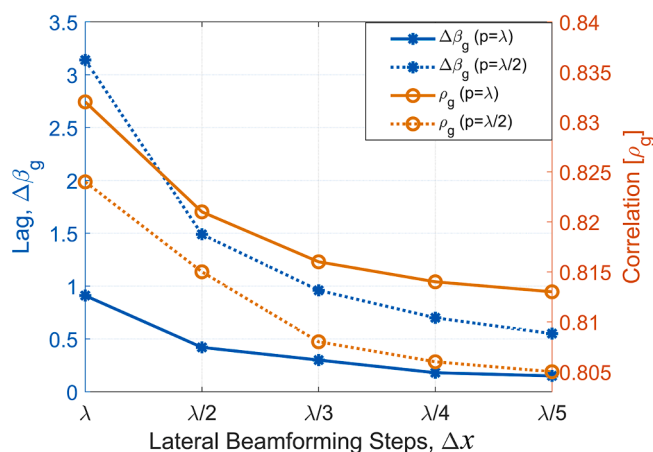


Fig. 2. Effect of reducing Δx was evaluated on probes with the pitch, $p = \lambda$ and $\lambda/2$ by measuring $\Delta\beta_g$ and ρ_g according to Eqs. (9) and (11).

The advantages or gains of reducing the Δx lies in the transducer with a larger pitch size starting from λ and above. Such transducer will optimize B-mode image quality simply by selecting the appropriate Δx . However, this approach is inapplicable to a smaller pitch size (not larger than $\lambda/2$). The low correlation among the adjacent aligned RF lines with the pitch size of $\lambda/2$ starting from the $\Delta x \lambda/2$ onwards as shown in Fig. 2, indicating that beamforming can be performed using the same Δx as the pitch size. No significant difference is observed if the RF signals obtained from the transducer with the pitch size of $\lambda/2$ is beamformed with a smaller Δx , such as $\lambda/3$, $\lambda/4$ or $\lambda/5$, because the correlation between adjacent RF lines is already low. The low correlation is an indication that the aligned RF signals for the second imaging line, become further apart from one another. This is a good indication such that when the process similar to autocorrelation takes place on the RF signals with a lower correlation value, noise cancellation will be higher on that particular imaging line.

4.2. Experimental results

The B-mode images of the point target and cyst phantom beamformed by using DAS and FDMAS (nine steering angles and a Δx of $\lambda/3$) are shown in Figs. 5 and 6. All the images are presented within a dynamic range of 50 dB. The point targets from depths of 20 mm to 60 mm beamformed with FDMAS achieve better results than those beamformed with DAS due to suppressed side lobes. The cysts located at depths of 15 mm and 45 mm obtain higher CR with FDMAS than DAS, because the high amount of clutter noise in the anechoic regions has been attenuated.

The LR results of the point target are presented in Figs. 7(a–d). The Δx is reduced from λ to $\lambda/5$, and thus the LR for FDMAS achieves 67.9% and 81.2% improvements at -6 dB and -20 dB, respectively for CPWI, $N = 9$. With the same Δx reduction, DAS achieves 54.8% and 67.4% improvements at -6 dB and -20 dB, respectively. However, most of the changes in LR for DAS only occur from λ to $\lambda/2$, whereas those for FDMAS occur from λ to $\lambda/3$. Beyond these values, improvements plateau at -6 dB and -20 dB. Side lobes are known to interfere with LR [33]. Thus, the LR of the main lobe is improved by attenuating the side lobes along the lateral direction. The concept behind this approach is clearly illustrated in the B-mode image and beam profiles as shown from Figs. 8–11. The B-mode image of point targets located at 40 mm and 50 mm depth are shown in Figs. 8 and 10 while their corresponding beam profiles are shown in Figs. 9 and 11 where noise reduction is notable in the lateral direction as the Δx is reduced from λ to $\lambda/5$. The energy in the side lobe regions is the main factor that affects the image contrast level [11,34]. Thus, attenuating side lobes more frequently through a process similar to autocorrelation with smaller $\Delta\beta_g$ helps improve image CR. The significant effect of sidelobe reduction along the lateral direction with FDMAS is illustrated in Fig. 8, row ii.

The results of CRs are presented in Fig. 12(a) and (b). The performance index shows the improvements when the Δx is reduced from λ to $\lambda/5$ for DAS and FDMAS. The CRs are improved by 4.18 dB and 10.38 dB for DAS and FDMAS, respectively for CPWI, $N = 9$.

The results of CNRs are presented in Fig. 12(c) and (d). As opposite to LR and CR, the CNR performance deteriorates when the Δx is reduced from λ to $\lambda/5$ for DAS and FDMAS. The CNRs decreased by 2.74 dB and 1.36 dB for DAS and FDMAS, respectively for CPWI, $N = 9$. This is expected due to more drop out regions in the speckle (i.e., black regions) that cause a higher variance (i.e., more noise) in the speckle, which therefore increases the denominator of the CNR equation when the Δx is reduced from λ to $\lambda/5$. The drop out regions could be potential problematic for the segmentation process because the active contour segmentation algorithms might think that a black region in the speckle is a cyst.

Higher CNR values are not main criteria for better segmentation process. The segmentation process which is initialized from the inside of

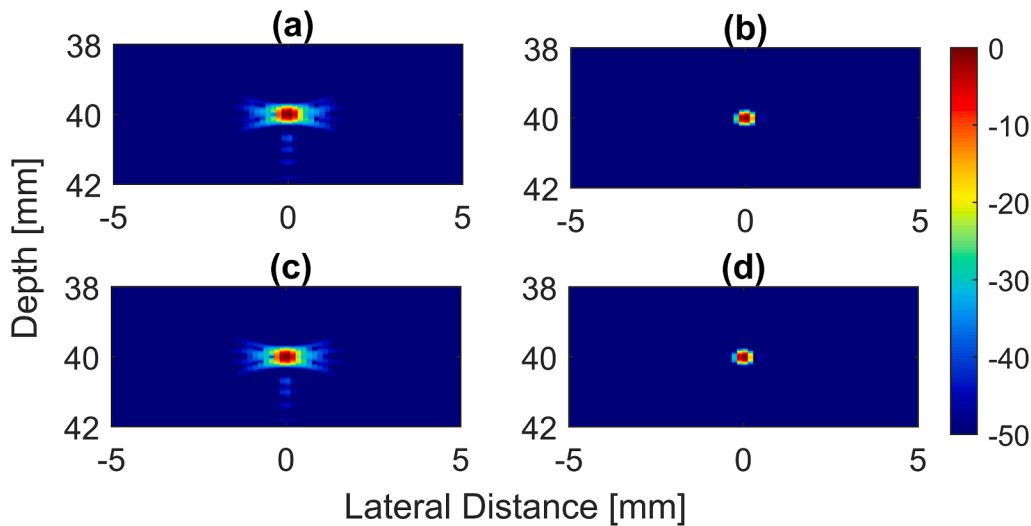


Fig. 3. B-mode images from CPWI, $N = 9$ for a point target located at 40 mm depth for the Δx of $\lambda/2$: a) DAS, $p = \lambda$, $E = 128$; b) FDMAS, $p = \lambda$, $E = 128$; c) DAS, $p = \lambda/2$, $E = 256$ and d) FDMAS, $p = \lambda/2$, $E = 256$.

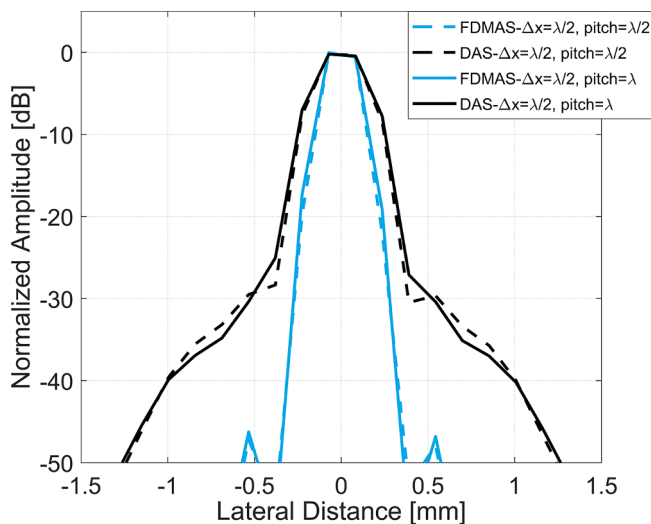


Fig. 4. Lateral beam profiles of a point target at a depth of 40 mm simulated using Field II using the pitch sizes, p of λ and $\lambda/2$ beamformed with the Δx of $\lambda/2$. The simulation parameters are identical to those in Table 3. Regardless of the pitch size, both beamforming techniques produced nearly similar results when beamformed with the same Δx . The legend represents the beamforming techniques-lateral beamforming step-pitch size.

the anechoic region such as a cyst does not depend on the speckle formation, but more on the level of clutter noise and CR. This is because the contour formation can be stopped by the false edge caused by clutter noise [35].

The leaking of the side lobes into the anechoic region also continues diminishing as the Δx is reduced from λ to $\lambda/5$. This phenomenon is illustrated in Fig. 13 which presents 1.3 mm-diameter cysts. As the Δx is reduced from λ to $\lambda/3$, the cyst edges become steeper due to side lobe reduction.

This can be seen from the lateral beam profiles shown in Fig. 14 for DAS and FDMAS. Side lobe reduction in the anechoic region from the Δx λ to $\lambda/3$ with FDMAS significantly improves BSAC segmentation on both cysts. The B-mode image and lateral beam profiles for a 3.0 mm-diameter cysts as the Δx reduced from λ to $\lambda/5$ are shown in Figs. 15 and 16.

Any low-quality B-mode image produced with the Δx of λ can be associated with beamforming that does not occur at the right location

where the point target is located. A pixel length in the x direction is equal to the λ , which is comparably longer than the exact length of the point target diameter, i.e. $120 \mu\text{m}$. Thus, a single grey colour intensity will be assigned through the λ length, which represents the Δx , but not the exact intensity on that location. One of the solutions for this problem is reducing the Δx used for beamforming.

Tables 4 and 5 presents the results obtained from a two-cycle sinusoidal excitation signal compounded with $N = 9$ and $N = 25$ for the Δx of $\lambda/2$ and $\lambda/3$. Only the values obtained with the two Δx were compared in this study because both values produced comparably good image quality. Moreover, only these values were compared to demonstrate that performance can be improved with less compounding angles when beamformed with a smaller Δx . All spatial and contrast performance indicators, except CNR produce better results with FDMAS, CPWI, $N = 9$ and the Δx of $\lambda/3$ instead of with FDMAS, CPWI, $N = 25$, and the Δx of $\lambda/2$. All the values that compare the compounding and Δx are highlighted in Tables 4 and 5 in bold typeface. From the results, a conclusion can be drawn that FDMAS generally needs lower compounding angles with a smaller Δx , which can improve the temporal resolution of B-mode images. The reduction of the number of compounding angles from $N = 25$ to $N = 9$ results in a 178% improvement in temporal resolution.

The main reason for the improvement in CR and CNR with the increased number of compounding angles is because the decorrelation between the side lobes that appear along the lateral direction. Each steered plane wave can be divided into two main components in general, the side lobe and main lobe. The side lobe appears at different spatial location for every steered plane wave whereas the main lobe appears almost at the same location for a particular point spread function. Thus, when coherent compounding takes place, noise cancellation mainly takes place for the side lobe. Beyond a certain number of compounding angles, the LR will not be improved but reduced since the main lobe broadens after the summation of contributions from different angles. The theory behind this is related to the beam directivity which determines the object appearance and shape in the compound image. The intensity distributions of steered plane waves are different for different angles. As the angle increases or decreases; the beam pattern and its intensity distribution are shifted accordingly. This phenomenon is mainly observed on the side lobes along the lateral direction.

4.3. Effect of reducing lateral beamforming step, Δx on segmentation

The sizes of the segmented cyst marked by green dashed lines as shown in Figs. 13 and 15 were measured and compared to their nominal

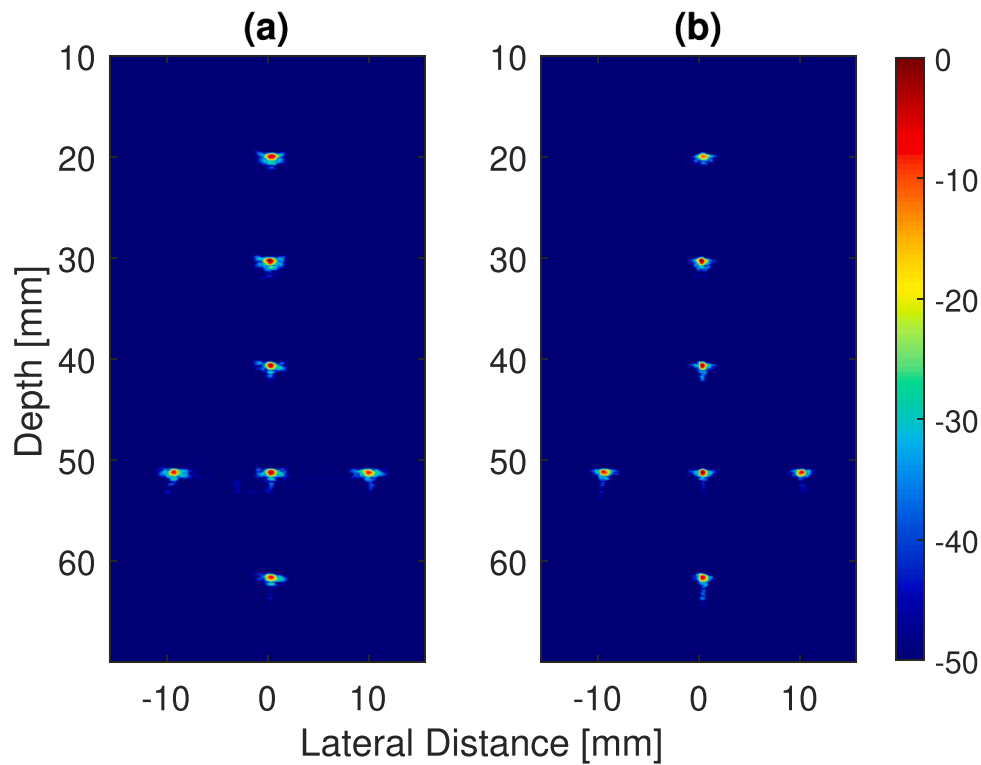


Fig. 5. B-Mode images of point targets beamformed with (a) DAS and (b) FDMAS, $N = 9$ with the Δx of $\lambda/3$.

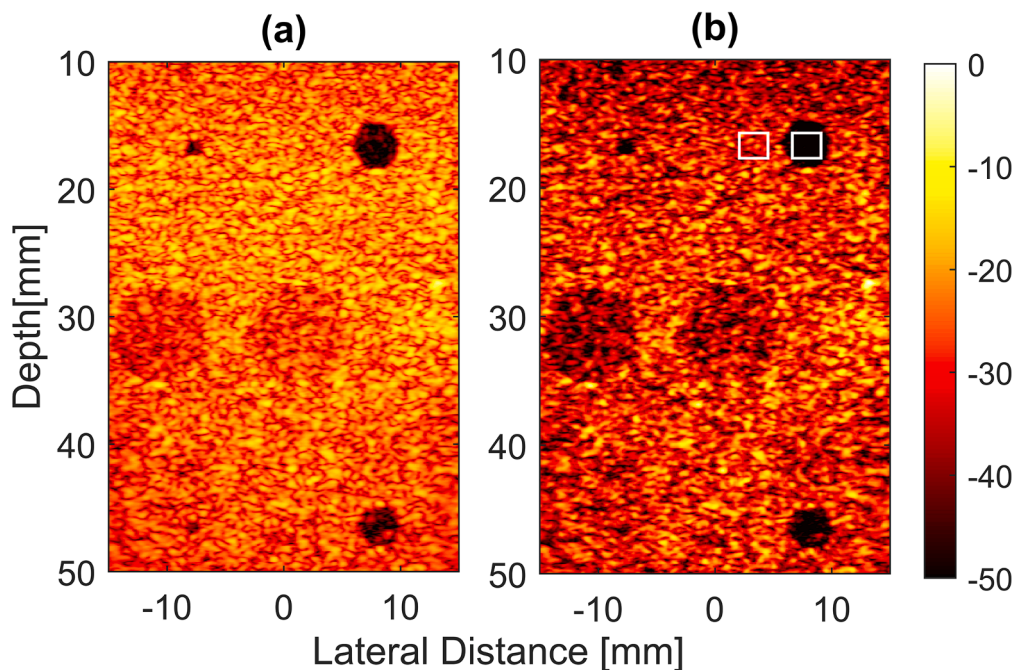


Fig. 6. B-mode images of cysts located at depths of 15 mm and 45 mm beamformed with (a) DAS and (b) FDMAS, $N = 9$ with the Δx of $\lambda/3$. Two regions with the same size, one inside and the other outside, as shown in (b) are selected to measure image CR.

values. To determine the region size, the number of pixels within the cyst was counted and multiplied with their corresponding lateral and axial pixel sizes. The axial pixel size was fixed to $9.625 \mu\text{m}$. The nominal cyst areas with the diameter of 1.3 mm and 3.0 mm are 1.33 mm^2 and 7.07 mm^2 , respectively. As shown in Fig. 17, the cyst sizes measured are approaching nominal values with FDMAS and lower Δx . This shows the

reduction of the Δx improves the BSAC-based segmentation process. The convergence time of the snake towards the cyst border covered by segmentation represented by the contour shown in green colour in Figs. 13 and 15 for 1.3 mm and 3.0 mm-diameter cysts was evaluated by fixing the number of iterations to 100 [36,37]. The total time needed for the snake to converge from the center of the object to the desired boundary

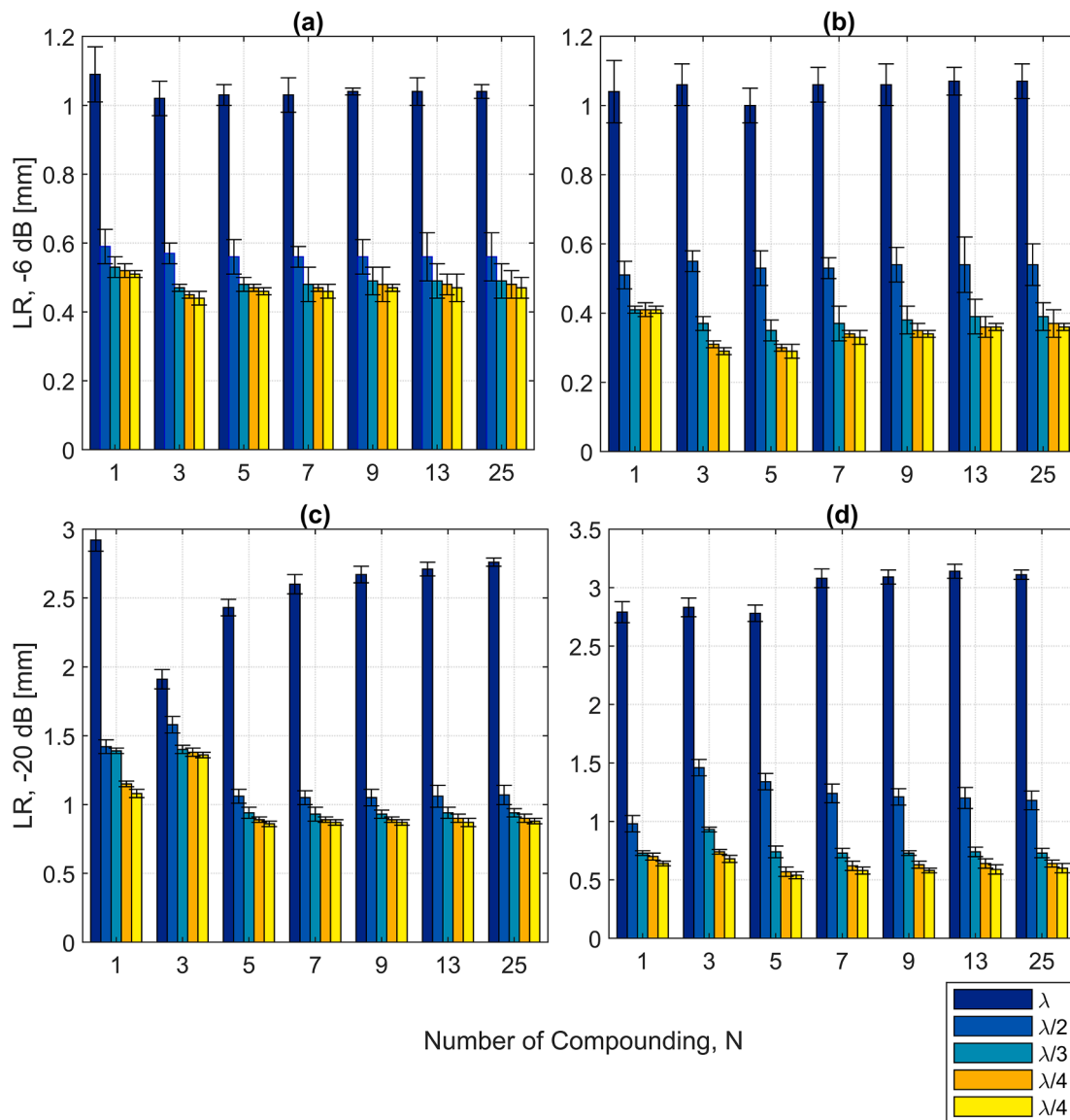


Fig. 7. LR performance at -6 dB: a) DAS and b) FDMAS, LR at -20 dB; c) DAS and d) FDMAS for CPWI from $N = 1$ to $N = 25$ as the Δx is reduced from λ to $\lambda/5$. The measurements were performed on a point target with a diameter of $120 \mu\text{m}$ at a depth of 40 mm. Results shown with the standard deviation error bars based on 10 measurements.

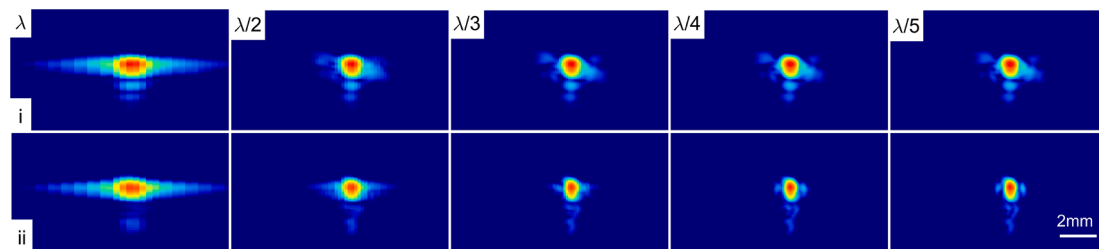


Fig. 8. B-mode images of point targets located at 40 mm depth beamformed with DAS (row i) and FDMAS (row ii) using different Δx ranging from λ to $\lambda/5$ and CPWI, $N = 9$. The colour map for the figure is the same as the one presented in Fig. 5. All the images are shown within a dynamic range of 50 dB.

depends on the amount of clutter noise present inside the object [38,39]. Longer time may be required when the snake fails to find its minimum energy due to the presence of high clutter noise inside the cysts region. Table 6 shows the amount of time needed for the snake to converge to the 1.3 mm and 3.0 mm-diameter cysts borders with DAS and FDMAS. The snake convergence time with DAS are higher than FDMAS for every

Δx . As the Δx reduced, the amount of time needed for the snake to converge is shorter with FDMAS. This shows that the reduction of the Δx reduced clutter noise present inside the cysts region and this cordially facilitates the snake to converge to the cyst border faster compared to larger Δx .

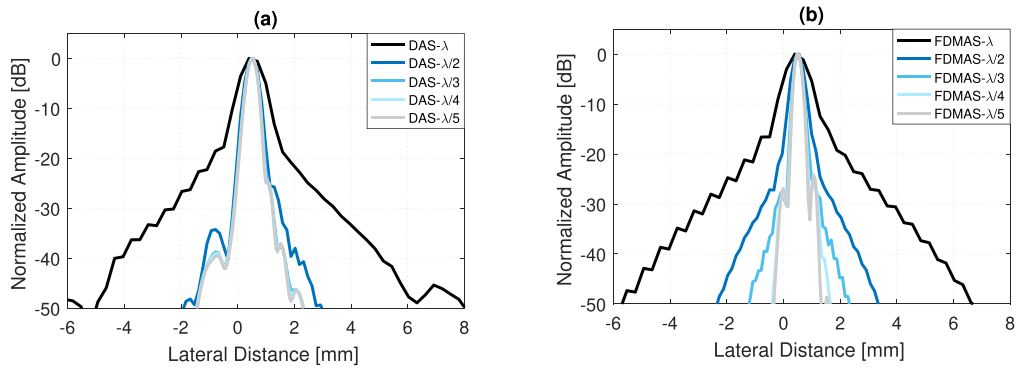


Fig. 9. Lateral beam profiles of the point targets located at 40 mm depth plotted for a) DAS and b) FDMAS beamforming techniques as the Δx starts to decrease from λ to $\lambda/5$ for CPWI, $N = 9$.

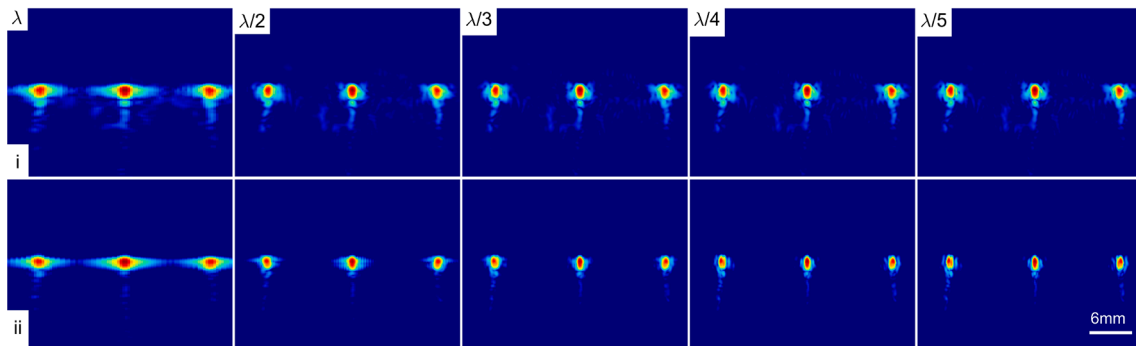


Fig. 10. B-mode images of point targets located at 50 mm depth beamformed with DAS (row i) and FDMAS (row ii) using different Δx ranging from λ to $\lambda/5$ and CPWI, $N = 9$. The colour map for the figure is the same as the one presented in Fig. 5. All the images are shown within a dynamic range of 50 dB.

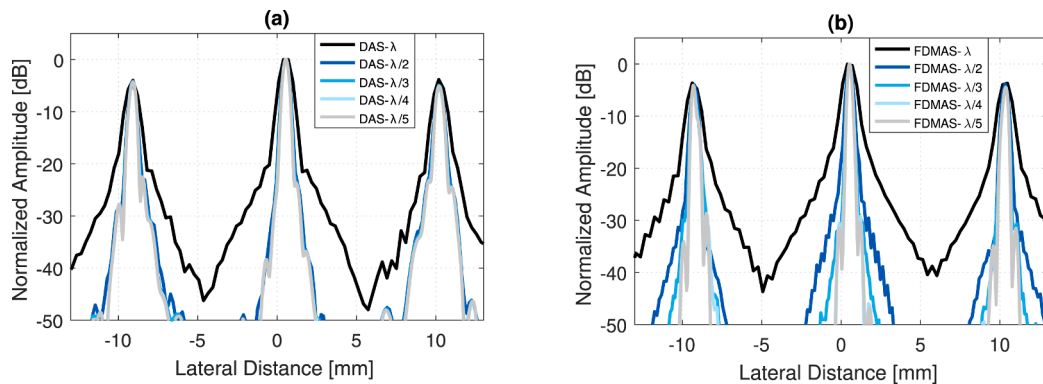


Fig. 11. Lateral beam profiles of the point targets located at 50 mm depth plotted for a) DAS and b) FDMAS beamforming techniques as the Δx starts to decrease from λ to $\lambda/5$ for CPWI, $N = 9$.

4.4. In vivo images

The performance of DAS and FDMAS with *in vivo* data was evaluated on the right side of one carotid artery. Clutter noise and side lobes are reduced as the Δx is reduced from λ to $\lambda/5$, facilitating enhancement of spatial and contrast resolutions with the FDMAS beamforming technique, as shown in Fig. 18, row ii. The side lobes leaking into the carotid artery anechoic regions demonstrate the same phenomenon observed in the cyst region shown in Fig. 15. However, the medium that surrounds the cyst border is uniformly composed of hyperechoic regions. Thus, the amount of side lobe signal leaking from the hyperechoic region to the anechoic region is less observable, although such leak also exists. However, the carotid artery presents a different case. The side lobes that are leaking into the carotid anechoic regions are caused by an extremely

strong hyperechoic medium. Thus, such leak becomes an obstacle to contour formation on the carotid boundary during the segmentation process. The speckle and clutter noise present in the B-mode image pose a challenge to the segmentation process which BSAC fails to converge to the intended boundary [40,41,39]. Thus, the reduction of clutter and side lobes in the carotid regions improves the segmentation process [42].

The 3D reconstruction of the carotid artery from the 2D transversal imaging also depends on a good segmentation output [43]. Thus, applying the segmentation output from FDMAS with a smaller Δx is expected to produce a good 3D carotid image.

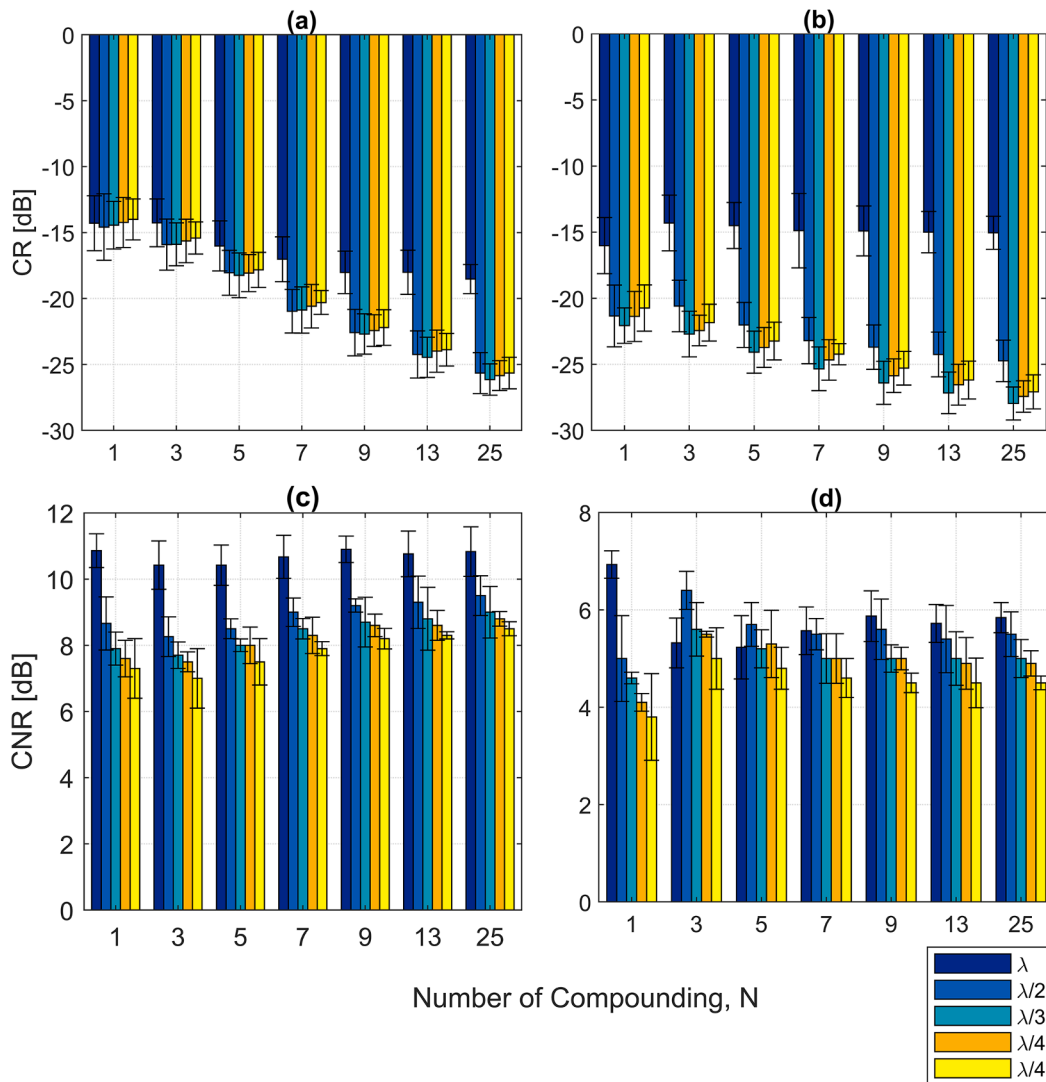


Fig. 12. CR performance: a) DAS and b) FDMAS, CNR; c) DAS and d) FDMAS for CPWI from $N = 1$ to $N = 25$ as the Δx is reduced from λ to $\lambda/5$. Both CR and CNR were computed on the 3.0-mm diameter cyst located at depth of 15 mm by creating two regions with the same dimension at same level as shown in Fig. 6. Results shown with the standard deviation error bars based on 10 measurements.

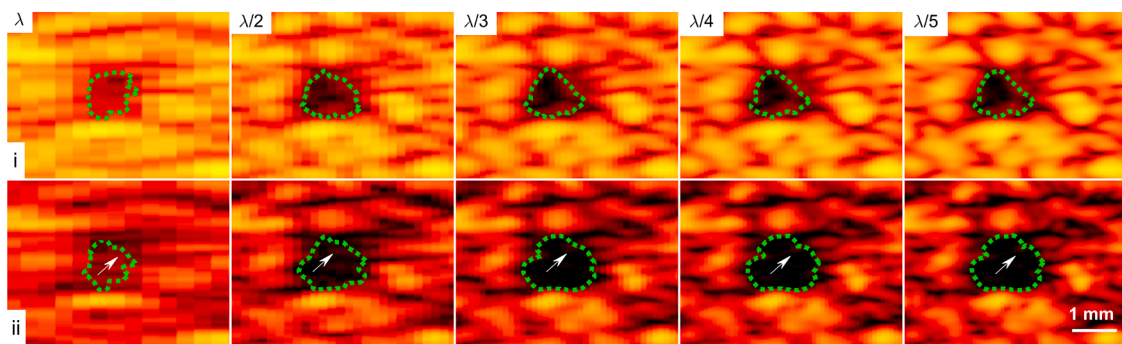


Fig. 13. CPWI, $N = 9$ B-mode images of a 1.3 mm-diameter cyst located at a depth of 15 mm beamformed with a Δx ranging from λ to $\lambda/5$ with (i) DAS and (ii) FDMAS. The contour of the cyst boundary shown in green dashed lines that represents the BSAC segmentation implemented on DAS and FDMAS continues to improve as the Δx starts to decrease. The arrows shown on the 2nd rows indicate the side lobe reduction in the lateral direction. The colour map for the figure is the same as that presented in Fig. 6. All the images are shown within a dynamic range of 50 dB.

5. Conclusion

In this study, the performance of DAS and FDMAS have been eval-

uated with CPWI, various pitch sizes, p , and lateral beamforming steps, Δx . The results clearly show that FDMAS produces better image quality than DAS when Δx is smaller than $\lambda/2$. The main observation from

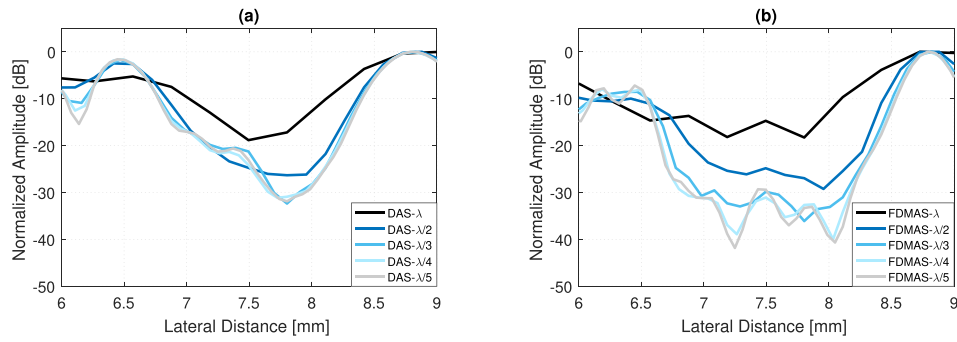


Fig. 14. Normalized lateral beam profiles of the 1.3 mm-diameter cyst at a depth of 15 mm with a) DAS and b) FDMAS from the Δx of λ to $\lambda/5$ for CPWI, $N = 9$.

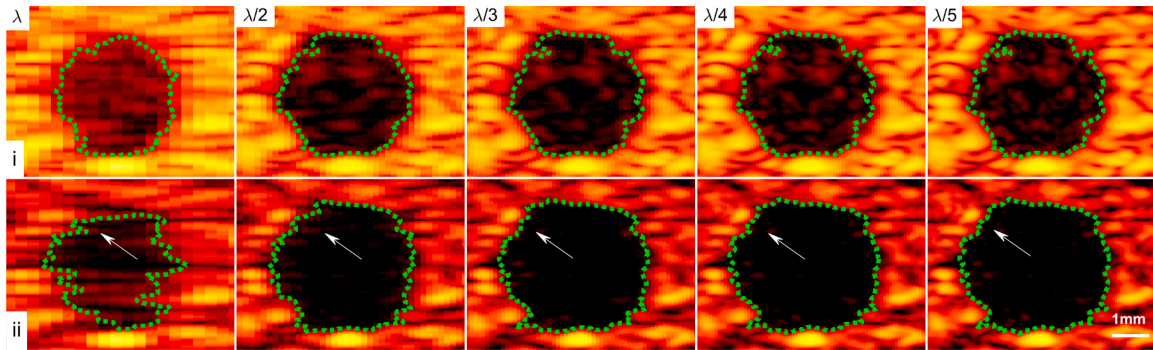


Fig. 15. CPWI, $N = 9$ B-mode images of a 3.0 mm-diameter cyst located at a depth of 15 mm beamformed with a Δx ranging from λ to $\lambda/5$ with (i) DAS and (ii) FDMAS. The contour of the cyst boundary shown in green dashed lines that represents the BSAC segmentation implemented on DAS and FDMAS continues to improve as the Δx starts to decrease. The arrows shown on the 2nd rows indicate the side lobe reduction in the lateral direction. The colour map for the figure is the same as that presented in Fig. 6. All the images are shown within a dynamic range of 50 dB.

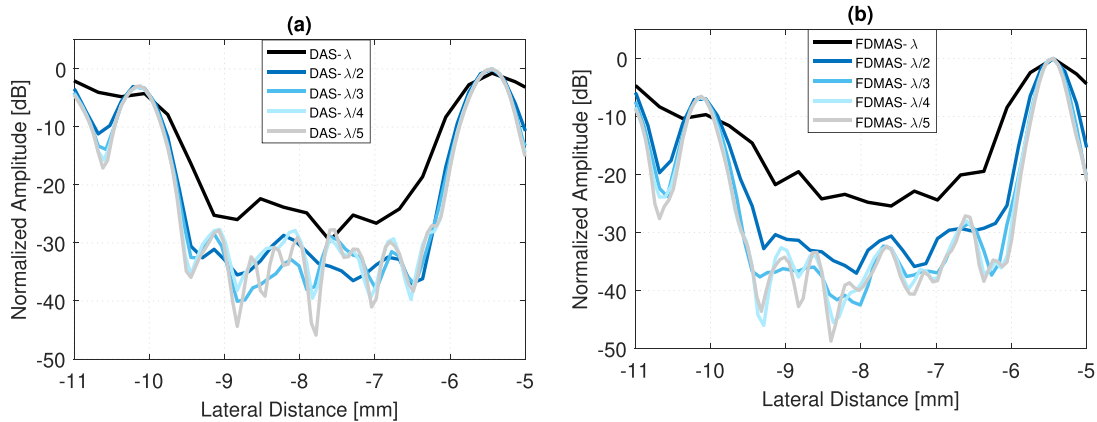


Fig. 16. Normalized lateral beam profiles of the 3.0 mm-diameter cyst at a depth of 15 mm with a) DAS and b) FDMAS from the Δx of λ to $\lambda/5$ for CPWI, $N = 9$.

Table 4
LR for DAS and FDMAS.

CPWI, N		LR, -6 dB [mm]		LR, -20 dB [mm]	
		$\lambda/2$	$\lambda/3$	$\lambda/2$	$\lambda/3$
9	DAS	0.56 ± 0.05	0.49 ± 0.04	1.05 ± 0.06	0.93 ± 0.03
	FDMAS	0.54 ± 0.05	0.38 ± 0.04	1.21 ± 0.07	0.73 ± 0.02
25	DAS	0.56 ± 0.07	0.49 ± 0.05	1.07 ± 0.07	0.94 ± 0.03
	FDMAS	0.54 ± 0.06	0.39 ± 0.04	1.18 ± 0.08	0.73 ± 0.04

Table 5
CR and CNR for DAS and FDMAS.

CPWI, N		CR [dB]		CNR [dB]	
		$\lambda/2$	$\lambda/3$	$\lambda/2$	$\lambda/3$
9	DAS	-22.58 ± 1.76	-22.69 ± 1.53	9.24 ± 0.2	8.68 ± 0.75
	FDMAS	-23.70 ± 1.68	-26.40 ± 1.63	5.59 ± 0.63	4.97 ± 0.28
25	DAS	-25.65 ± 1.55	-26.14 ± 1.19	9.47 ± 0.6	8.96 ± 0.78
	FDMAS	-24.74 ± 1.57	-27.96 ± 1.25	5.47 ± 0.46	4.97 ± 0.39

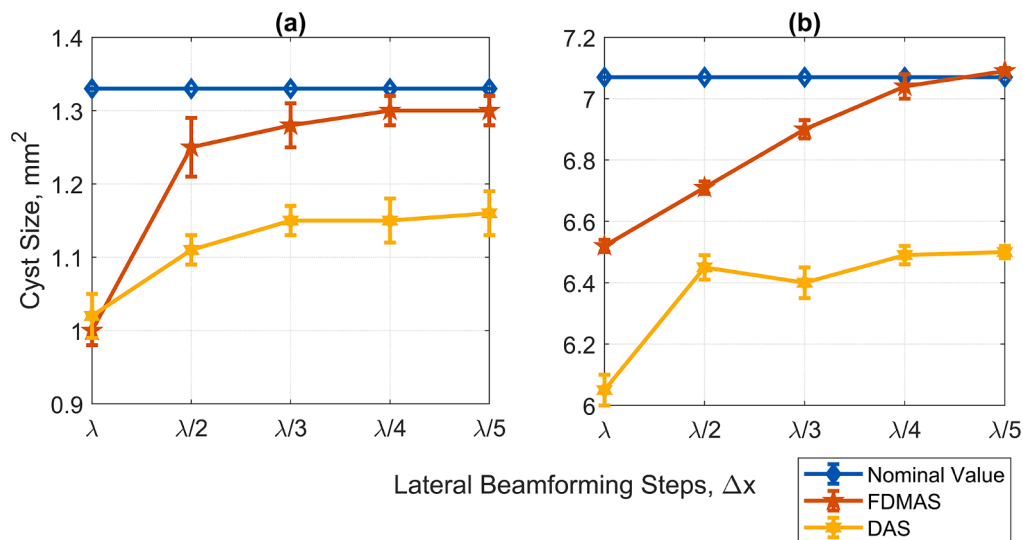


Fig. 17. The region covered by segmentation represented by the contour shown in green colour in Figs. 13 and 15 measured for (a) 1.3 mm and (b) 3.0 mm-diameter cysts. Results shown with the standard deviation error bars based on 10 measurements.

Table 6

Snake convergence time, in seconds for 100 iterations.

Properties	Values				
	λ	$\lambda/2$	$\lambda/3$	$\lambda/4$	$\lambda/5$
DAS, 1.3 mm	4.7 ± 0.5	4.6 ± 0.4	4.6 ± 0.5	4.6 ± 0.3	4.6 ± 0.3
FDMAS, 1.3 mm	4.5 ± 0.3	4.1 ± 0.1	3.2 ± 0.1	3.1 ± 0.2	3.1 ± 0.1
DAS, 3.0 mm	6.0 ± 0.5	5.8 ± 0.6	5.8 ± 0.3	5.7 ± 0.4	5.8 ± 0.3
FDMAS, 3.0 mm	5.1 ± 0.2	4.6 ± 0.1	4.3 ± 0.1	4.1 ± 0.2	4.0 ± 0.3

reducing the Δx is that the performance of FDMAS is improved when the process similar to autocorrelation occurs with a smaller step. The multiplication and addition of RF signals with a smaller Δx further attenuated clutter noise, which can increase image CR. Attenuating clutter noise also makes the CNR value a little deteriorated. Although reducing Δx from λ to $\lambda/5$ improves image quality, the most significant improvement occurs between λ and $\lambda/3$. Thus, $\lambda/3$ is selected for FDMAS to optimize beamforming processing time. This work found that a high frame rate can be achieved without sacrificing image spatial and contrast resolutions when the received RF signal is beamformed with

FDMAS at a smaller Δx . The BSAC segmentation applied to FDMAS exhibits significant improvement as Δx is reduced from λ to $\lambda/5$. A small CNR does not affect the segmentation process since the CR and LR parameters play much important roles in contour formation. The boundary definition is improved because the side lobes leaking into the anechoic region are reduced. Thus, FDMAS beamforming technique will be beneficial for segmentation purposes and other beamforming technique such as DAS could be suitable for better anatomical viewing.

CRediT authorship contribution statement

Asraf Mohamed Moubark: Conceptualization, Methodology, Software, Writing - original draft. Zainab Alomari: Software, Validation. Mohd Hairi Mohd Zaman: Visualization, Investigation. Mohd Asyraf Zulkifley: Visualization, Investigation. Sawal Hamid Md Ali: Visualization, Investigation. Luzhen Nie: Supervision, Writing - review & editing. Steven Freear: Supervision, Writing - review & editing.

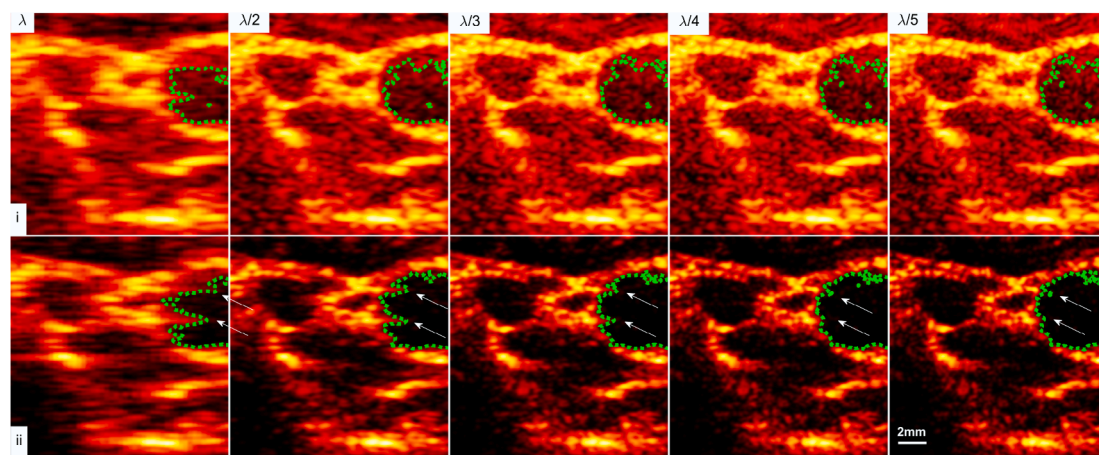


Fig. 18. Carotid artery B-mode images obtained with a two-cycle sinusoidal excitation signal and nine compounding angles beamformed from the Δx of λ to $\lambda/5$ with DAS (row i) and FDMAS (row ii). The arrows shown on the 2nd rows indicate the side lobe reduction in the lateral direction as the Δx is reduced. This improves the boundary formation with the segmentation process on CCA. The colour map in the figure is the same as the one presented in Fig. 6. All the images are shown within a dynamic range of 50 dB.

Declaration of Competing Interest

The authors declare that they have no known competing financial interests or personal relationships that could have appeared to influence the work reported in this paper.

Acknowledgement

This research was funded by Ministry of Higher Education Malaysia, under Grant No. FRGS/1/2019/TK04/UKM/03/4. Funders were not involved in the conduct of the research.

References

- [1] A.M. Moubark, S. Harput, D.M.J. Cowell, S. Freear, Clutter noise reduction in B-Mode image through mapping and clustering signal energy for better cyst classification, *IEEE International Ultrasonics Symposium (IUS) 2016* (2016) 1–4, <https://doi.org/10.1109/ULTSYM.2016.7728860>.
- [2] M.A. Lediju, M.J. Pihl, J.J. Dahl, G.E. Trahey, Quantitative assessment of the magnitude, impact and spatial extent of ultrasonic clutter, *Ultrason. Imaging* 30 (3) (2008) 151–168.
- [3] A.M. Moubark, Z. Alomari, S. Harput, D.M.J. Cowell, S. Freear, Enhancement of contrast and resolution of B-mode plane wave imaging (PWI) with non-linear filtered delay multiply and sum (FDMAS) beamforming, in: *2016 IEEE International Ultrasonics Symposium (IUS)*, 2016, pp. 1–4.
- [4] B.M. Asl, A. Mahloojifar, A low-complexity adaptive beamformer for ultrasound imaging using structured covariance matrix, *IEEE Trans. Ultrason. Ferroelectr. Freq. Control* 59 (4) (Apr. 2012) 660–667, <https://doi.org/10.1109/TUFFC.2012.2244>.
- [5] J. Zhao, Y. Wang, J. Yu, W. Guo, S. Zhang, S. Aliabadi, Short-lag Spatial Coherence Ultrasound Imaging with Adaptive Synthetic Transmit Aperture Focusing, *Ultrason. Imaging* 39 (4) (2017) 224–239, <https://doi.org/10.1177/0161734616688328>.
- [6] H.B. Lim, N.T.T. Nhung, E.P. Li, N.D. Thang, Confocal Microwave Imaging for Breast Cancer Detection: Delay-Multiply-and-Sum Image Reconstruction Algorithm, *IEEE Trans. Biomed. Eng.* 55 (6) (Jun. 2008) 1697–1704, <https://doi.org/10.1109/TBME.2008.919716>.
- [7] M. Klemm, L.J. Craddock, J.A. Leendertz, A. Preece, R. Benjamin, Improved delay-and-sum beamforming algorithm for breast cancer detection, *Int. J. Antennas Propag. vol* (2008) 2008.
- [8] M. Lazebnik, et al., A large-scale study of the ultrawideband microwave dielectric properties of normal breast tissue obtained from reduction surgeries, *Phys. Med. Biol.* 52 (10) (2007) 2637.
- [9] M. Klemm, J.A. Leendertz, D. Gibbins, L.J. Craddock, A. Preece, R. Benjamin, Microwave Radar-Based Breast Cancer Detection: Imaging in Inhomogeneous Breast Phantoms, *IEEE Antennas Wirel. Propag. Lett.* 8 (2009) 1349–1352, <https://doi.org/10.1109/LAWP.2009.2036748>.
- [10] E.C. Fear, X. Li, S.C. Hagness, M.A. Stuchly, Confocal microwave imaging for breast cancer detection: localization of tumors in three dimensions, *IEEE Trans. Biomed. Eng.* 49 (8) (Aug. 2002) 812–822, <https://doi.org/10.1109/TBME.2002.800759>.
- [11] G. Matrone, A.S. Savoia, G. Caliano, G. Magenes, The Delay Multiply and Sum Beamforming Algorithm in Ultrasound B-Mode Medical Imaging, *IEEE Trans. Med. Imaging* 34 (4) (Apr. 2015) 940–949, <https://doi.org/10.1109/TMI.2014.2371235>.
- [12] I.K. Holfort, A. Austeng, J.F. Synnevåg, S. Holm, F. Gran, J.A. Jensen, Adaptive receive and transmit apodization for synthetic aperture ultrasound imaging, in: *2009 IEEE International Ultrasonics Symposium*, 2009, pp. 1–4, <https://doi.org/10.1109/ULTSYM.2009.5442035>.
- [13] G. Matrone, A.S. Savoia, G. Caliano, G. Magenes, Ultrasound plane-wave imaging with delay multiply and sum beamforming and coherent compounding, in: *2016 38th Annual International Conference of the IEEE Engineering in Medicine and Biology Society (EMBC)*, 2016, pp. 3223–3226, <https://doi.org/10.1109/EMBC.2016.7591415>.
- [14] G. Matrone, A. Ramalli, A.S. Savoia, P. Tortoli, G. Magenes, High Frame-Rate, High Resolution Ultrasound Imaging With Multi-Line Transmission and Filtered-Delay Multiply And Sum Beamforming, *IEEE Trans. Med. Imaging* 36 (2) (2017) 478–486, <https://doi.org/10.1109/TMI.2016.2615069>.
- [15] G. Matrone, A.S. Savoia, G. Caliano, G. Magenes, Depth-of-field enhancement in Filtered-Delay Multiply and Sum beamformed images using Synthetic Aperture Focusing, *Ultrasonics* 75 (2017) 216–225.
- [16] J. Jensen, M.B. Stuart, J.A. Jensen, Optimized Plane Wave Imaging for Fast and High-Quality Ultrasound Imaging, *IEEE Trans. Ultrason. Ferroelectr. Freq. Control* 63 (11) (2016) 1922–1934, <https://doi.org/10.1109/TUFFC.2016.2591980>.
- [17] M. Kass, A. Witkin, D. Terzopoulos, Snakes: Active contour models, *Int. J. Comput. Vis.* 1 (4) (1988) 321–331.
- [18] A. Chaudhry, M. Hassan, A. Khan, J.Y. Kim, Automatic active contour-based segmentation and classification of carotid artery ultrasound images, *J. Digit. Imaging* 26 (6) (2013) 1071–1081.
- [19] A.K. Jumaat, et al., Performance comparison of Canny and Sobel edge detectors on Balloon Snake in segmenting masses, in: *2014 International Conference on Computer and Information Sciences (ICCOINS)*, 2014, pp. 1–5, <https://doi.org/10.1109/ICCOINS.2014.6868368>.
- [20] B. Das, S. Banerjee, *Parametric contour model in medical image segmentation*, in: *Deformable Models*, Springer, 2007, pp. 31–74.
- [21] F. Molinari, G. Zeng, J.S. Suri, A state of the art review on intima-media thickness (IMT) measurement and wall segmentation techniques for carotid ultrasound, *Comput. Methods Programs Biomed.* 100 (3) (2010) 201–221, <https://doi.org/10.1016/j.cmpb.2010.04.007>.
- [22] A. Austeng, C.I.C. Nilsen, A.C. Jensen, S.P. Næsholm, S. Holm, Coherent plane-wave compounding and minimum variance beamforming, in: *2011 IEEE International Ultrasonics Symposium*, 2011, pp. 2448–2451, <https://doi.org/10.1109/ULTSYM.2011.0608>.
- [23] M. Toulemonde, O. Basset, P. Tortoli, C. Cachard, Thomson's multitaper approach combined with coherent plane-wave compounding to reduce speckle in ultrasound imaging, *Ultrasonics* 56 (2015) 390–398.
- [24] G. Montaldo, M. Tanter, J. Bercoff, N. Benez, M. Fink, Coherent plane-wave compounding for very high frame rate ultrasonography and transient elastography, *IEEE Trans. Ultrason. Ferroelectr. Freq. Control* 56 (3) (2009) 489–506, <https://doi.org/10.1109/TUFFC.2009.1067>.
- [25] Z. Alomari, S. Harput, S. Hyder, S. Freear, Selecting the number and values of the CPWI steering angles and the effect of that on imaging quality, *IEEE International Ultrasonics Symposium 2014* (2014) 1191–1194, <https://doi.org/10.1109/ULTSYM.2014.0293>.
- [26] D. Ruchkin, Error of correlation coefficient estimates from polarity coincidences (corresp.), *IEEE Trans. Inf. Theory* 11 (2) (1965) 296–297.
- [27] J. Harrington, S. Cassidy, *Techniques in Speech Acoustics*, vol. 8, Springer Science & Business Media, 2012.
- [28] D.M.J. Cowell, S. Freear, Quinary excitation method for pulse compression ultrasound measurements, *Ultrasonics* 48 (2) (2008) 98–108.
- [29] P.R. Smith, D.M.J. Cowell, B. Raiton, C.V. Ky, and S. Freear, Ultrasound array transmitter architecture with high timing resolution using embedded phase-locked loops, *IEEE Trans. Ultrason. Ferroelectr. Freq. Control* 59 (1) (2012) 40–49, doi: 10.1109/TUFFC.2012.2154.
- [30] D.M.J. Cowell, T. Carpenter, P. Smith, C. Adams, S. Harput, S. Freear, Performance of switched mode arbitrary excitation using Harmonic Reduction Pulse Width Modulation (HRPWM) in array imaging applications, in: *2016 IEEE International Ultrasonics Symposium (IUS)*, 2016, pp. 1–4, <https://doi.org/10.1109/ULTSYM.2016.7728816>.
- [31] S. Harput, J. McLaughlan, D.M.J. Cowell, S. Freear, New performance metrics for ultrasound pulse compression systems, in: *2014 IEEE International Ultrasonics Symposium*, 2014, pp. 440–443, <https://doi.org/10.1109/ULTSYM.2014.0109>.
- [32] J.A. Jensen, N.B. Svendsen, Calculation of pressure fields from arbitrarily shaped, apodized, and excited ultrasound transducers, *IEEE Trans. Ultrason. Ferroelectr. Freq. Control* 39 (2) (1992) 262–267, <https://doi.org/10.1109/58.139123>.
- [33] J.P. Lawrence, Physics and instrumentation of ultrasound, *Crit. Care Med.* 35 (8) (2007) S314–S322.
- [34] T. Misaridis, J.A. Jensen, Use of modulated excitation signals in medical ultrasound. Part III: high frame rate imaging, *IEEE Trans. Ultrason. Ferroelectr. Freq. Control* 52 (2) (2005) 208–219, doi: 10.1109/TUFFC.2005.1406547.
- [35] J. De Vylder, J. Aelterman, W. Philips, Robust active contour segmentation with an efficient global optimizer, in: *International Conference on Advanced Concepts for Intelligent Vision Systems*, 2011, pp. 195–206.
- [36] Y. Song, G. Peng, A fast two-stage active contour model for intensity inhomogeneous image segmentation, *PLoS One* 14 (4) (2019), e0214851.
- [37] S. Soomro, A. Munir, K.N. Choi, Hybrid two-stage active contour method with region and edge information for intensity inhomogeneous image segmentation, *PLoS One* 13 (1) (2018), e0191827.
- [38] L. Álvarez, L. Baumela, P. Henriques, P. Márquez-Neila, Morphological snakes, in: *2010 IEEE Computer Society Conference on Computer Vision and Pattern Recognition*, 2010, pp. 2197–2202.
- [39] A. Khadidos, V. Sanchez, C.-T. Li, Active contours based on weighted gradient vector flow and balloon forces for medical image segmentation, in: *2014 IEEE International Conference on Image Processing (ICIP)*, 2014, pp. 902–906.
- [40] G. Slabaugh, G. Unal, M. Wels, T. Fang, B. Rao, Statistical region-based segmentation of ultrasound images, *Ultrasound Med. Biol.* 35 (5) (2009) 781–795.
- [41] G. Zhu, S. Zhang, Q. Zeng, C. Wang, Gradient vector flow active contours with prior directional information, *Pattern Recognit. Lett.* 31 (9) (2010) 845–856.
- [42] J.R.H. Kumar, C.S. Seelamantula, N.S. Narayan, P. Marziliano, Automatic segmentation of common carotid artery in transverse mode ultrasound images, in: *2016 IEEE International Conference on Image Processing (ICIP)*, 2016, pp. 389–393, <https://doi.org/10.1109/ICIP.2016.7532385>.
- [43] E. Yeom, K.-H. Nam, C. Jin, D.-G. Paeng, S. Lee, 3D reconstruction of a carotid bifurcation from 2D transversal ultrasound images, *Ultrasonics* 54 (8) (2014) 2184–2192.
- [44] Z.R.S. Alomari, Plane wave imaging beamforming techniques for medical ultrasound imaging, University of Leeds, 2017.
- [45] S. Korukonda, Application of synthetic aperture imaging to noninvasive vascular elastography, University of Rochester, 2012.